

## CHAPTER 4 RESULTS

### 4.1 Ti-46Al and Ti-48Al alloys

#### 4.1.1 As-cast macrostructures and microstructures

Observations of the macrostructure at the top surfaces of the button-shaped specimens of Ti-Al and Ti-Al-Nb alloys (Figure 4.1) revealed that the direction of the macrostructure morphology of both alloys are directional (from side to center) possible solidification paths for all of the alloys, corresponding to the phase diagrams of Ti-Al and Ti-Al-Nb, are shown in Figure 2.9, are as follows;  $L \rightarrow \alpha$ ,  $\alpha \rightarrow \alpha + \gamma$  and  $\alpha + \gamma \rightarrow \alpha_2 + \gamma$ . With respect to the morphologies of the top surfaces (Figure 4.2), the binary Ti-46Al and Ti-48Al have dendrite sizes larger than those of the ternary Ti-46Al and Ti-48Al with 5 and 10 at.% Nb. Additionally, smaller dendrite sizes were found in the 10% at. Nb addition (Table 4.1).

**Table 4.1** Dendrite sizes of experimental alloys

Alloys	Dendrite size ( $\mu\text{m}$ )
Ti-46Al	86-188
Ti-48Al	82-212
Ti-46Al-5Nb	26-58
Ti-48Al-5Nb	24-68
Ti-46Al-10Nb	16-43
Ti-48Al-10Nb	28-47

Figure 4.3 shows the macrostructures of all of the alloys. For the Ti-46Al binary alloy, it was found that the columnar equiaxed structures were oriented along the horizontal

direction toward the center of the button specimen. For the specimens with additions of 5 at.%Nb into the Ti-46Al alloy, a randomly oriented fine columnar structure with large equiaxed zone was observed. For the Ti-48Al binary and ternary alloys with additions of 5 and 10 Nb (at.%), only a fine columnar structure was identified.

The as-cast microstructures are shown in Figure 4.4. All of the alloys have a lamellar structure. A fully lamellar structure was found in the Ti-46Al-10Nb ternary alloys (Figure 4.4 (c)). Finer lamellar structures were found in the Ti-48Al-10Nb ternary alloy. The Ti-48Al binary and ternary (with Nb) alloys possess finer lamellae than the Ti-46Al binary and ternary alloys.

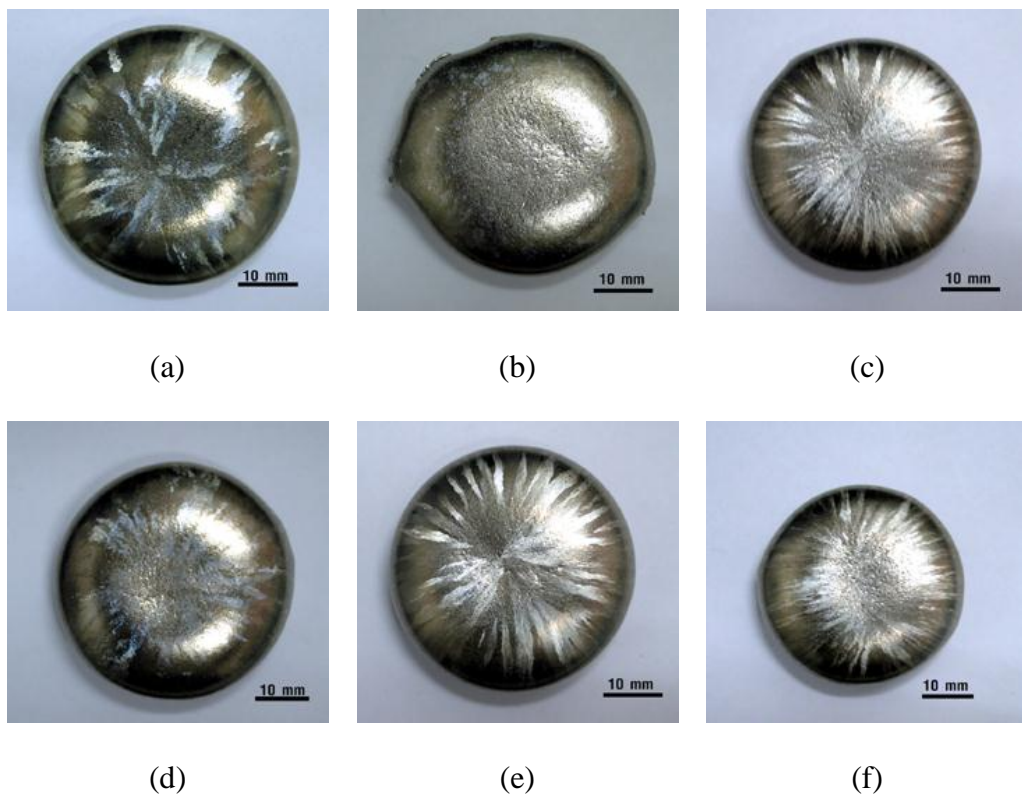


**Figure 4.1** Button-shaped specimens: (a) Ti-46Al, (b) Ti-46Al-5Nb,  
(c) Ti-46Al-10Nb, (d) Ti-48Al, (e) Ti-48Al-5Nb, (f) Ti-48Al-10Nb

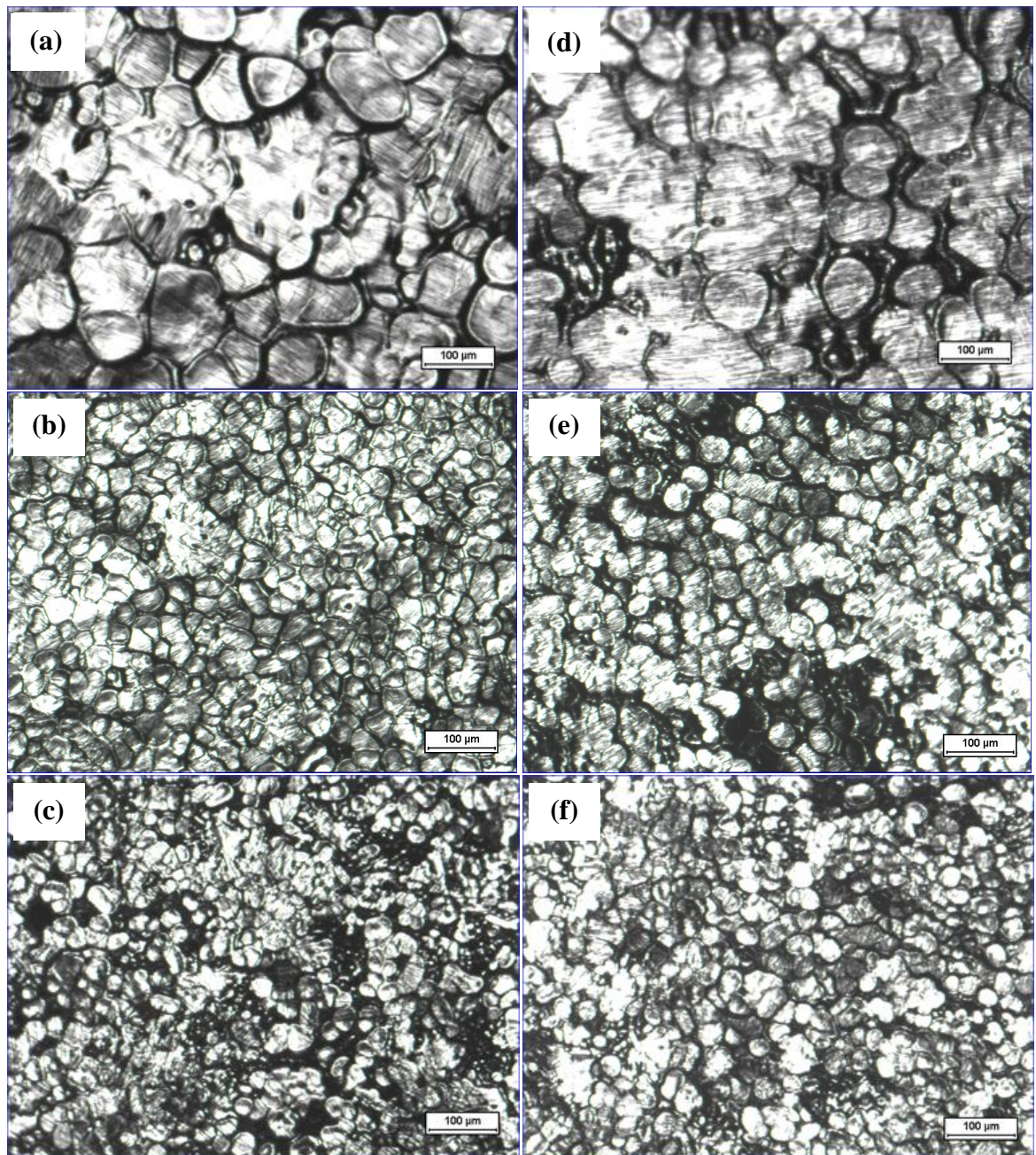


**Figure 4.2** Optical micrographs of the top surfaces, illustrating dendrite structures and microstructures of various alloy compositions: (a) Ti-46Al, (b) Ti-46Al-5Nb, (c) Ti-46Al-10Nb, (d) Ti-48Al, Ti-48Al, (e) Ti-48Al-5Nb, (f) Ti-48Al-10Nb.

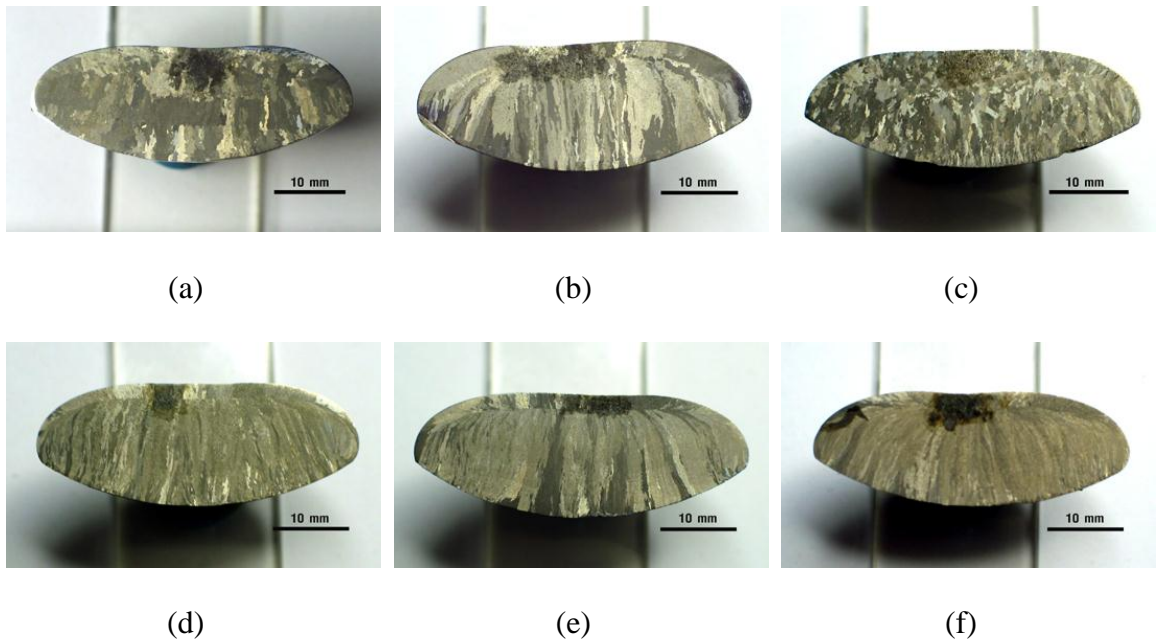


**Figure 4.3** Partially melted arc-melted ingots. (a) Ti-46Al, (b) Ti-46Al-5Nb, (c) Ti-46Al-10Nb, (d) Ti-48Al, (e) Ti-48Al-5Nb, (f) Ti-48Al-10Nb.

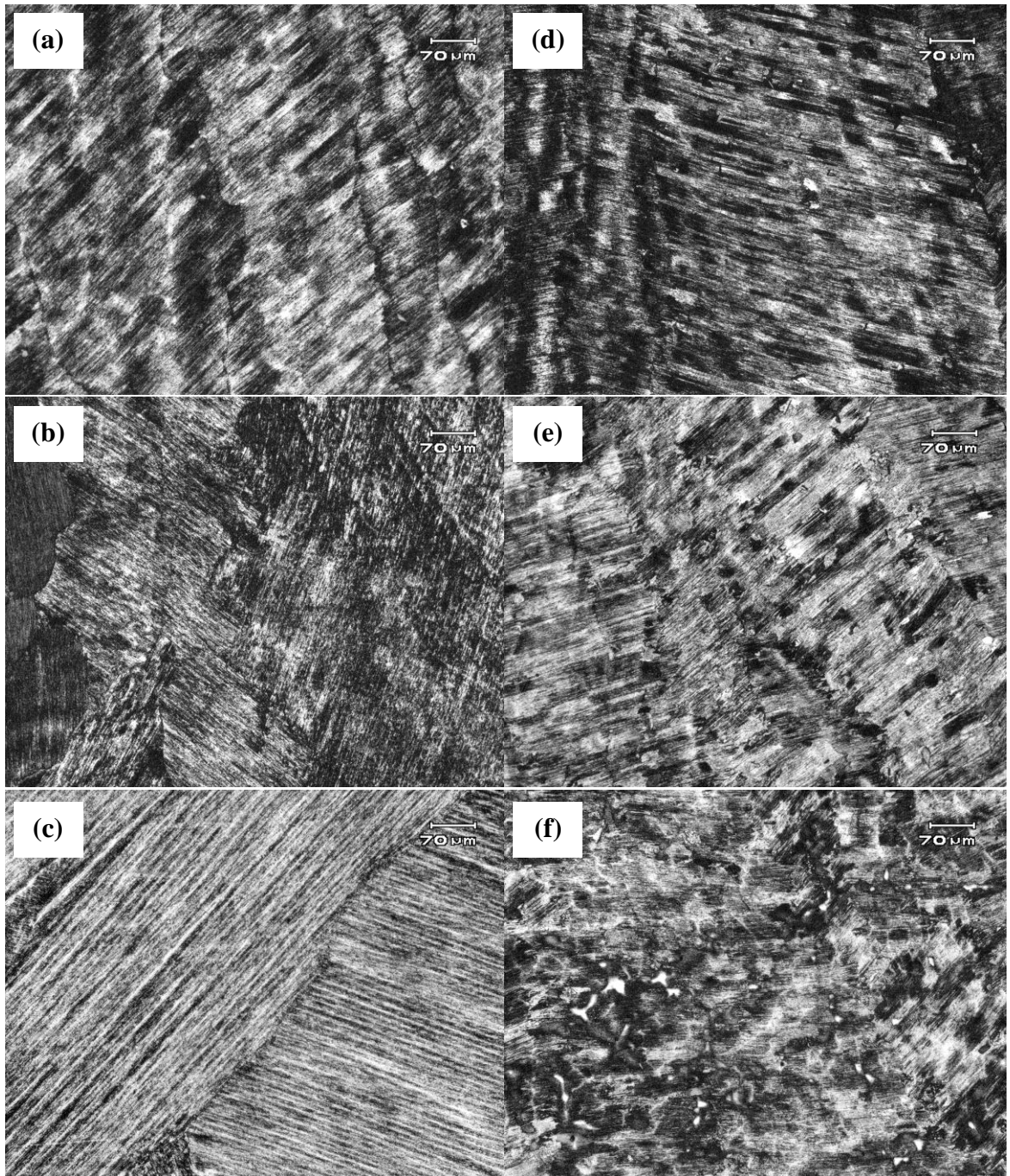


**Figure 4.4** As-cast microstructures of the Ti-Al and Ti-Al-Nb alloys. (a) Ti-46Al, (b) Ti-46Al-5Nb, (c) Ti-46Al-10Nb, (d) Ti-48Al, (e) Ti-48Al-5Nb, (f) Ti-48Al-10Nb.

### 4.1.2 X-ray diffraction results

Figures 4.5 - 4.10 show X-ray diffraction patterns of the as-cast structures of Ti-46Al, Ti-46Al-5Nb, Ti-46Al-10Nb, Ti-48Al, Ti-48Al-5Nb, and Ti-48Al-10Nb. The pattern reveals the presence of  $\gamma$ -TiAl as well as a small fraction of  $\alpha_2$ -Ti<sub>3</sub>Al in the Ti-46Al and Ti-48Al binary and ternary alloys.

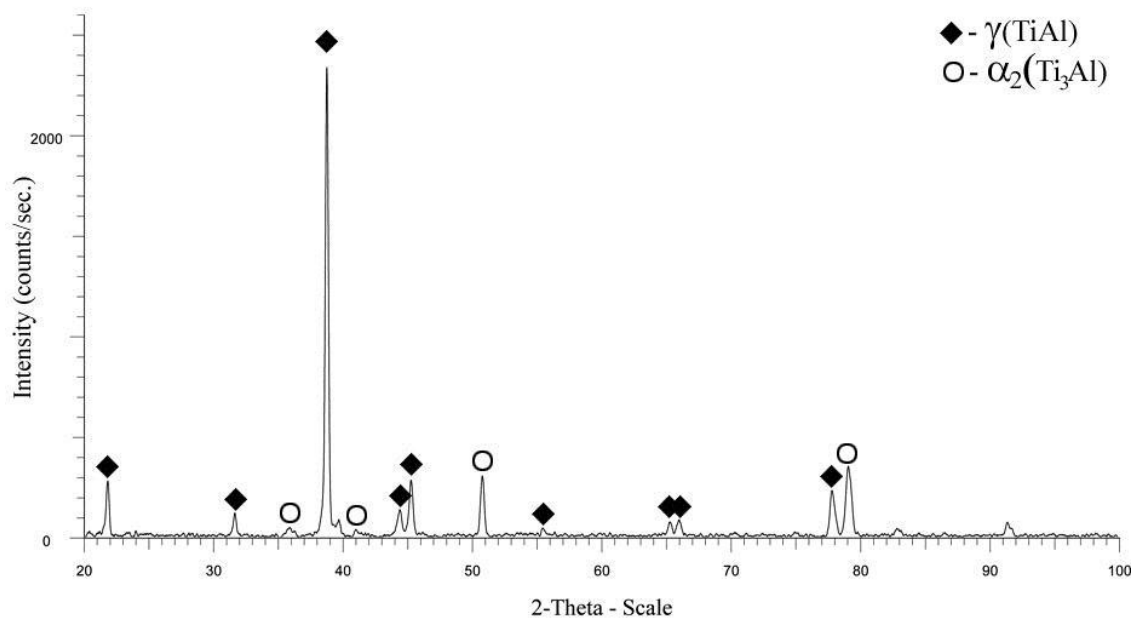


**Figure 4.5** XRD pattern of Ti-46Al

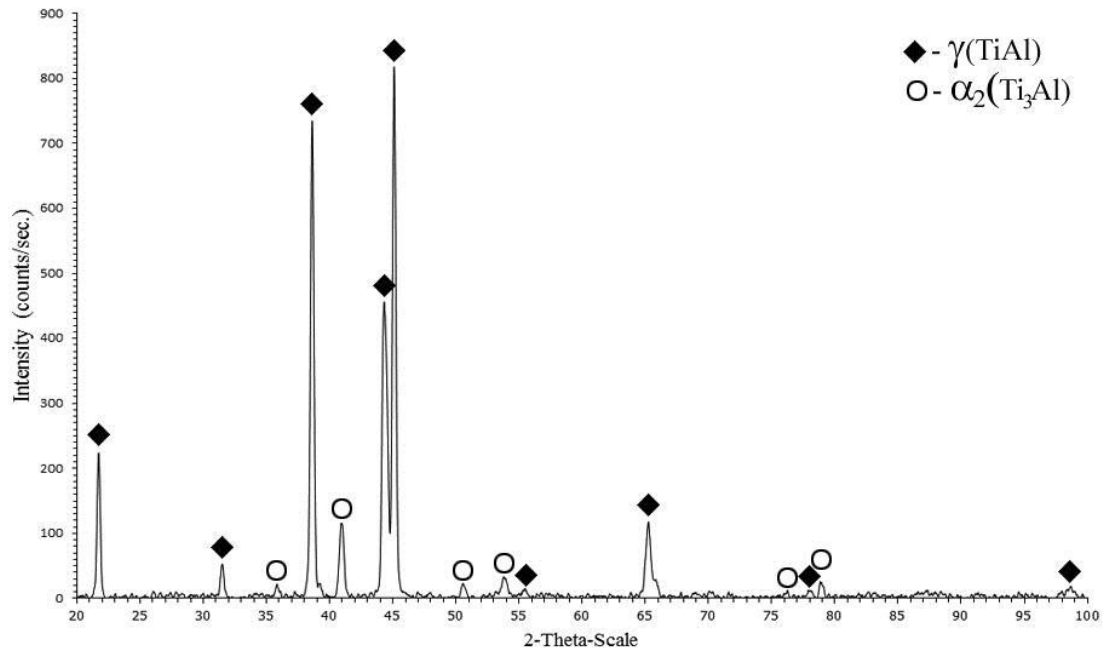


**Figure 4.6** XRD pattern of Ti-46Al-5Nb

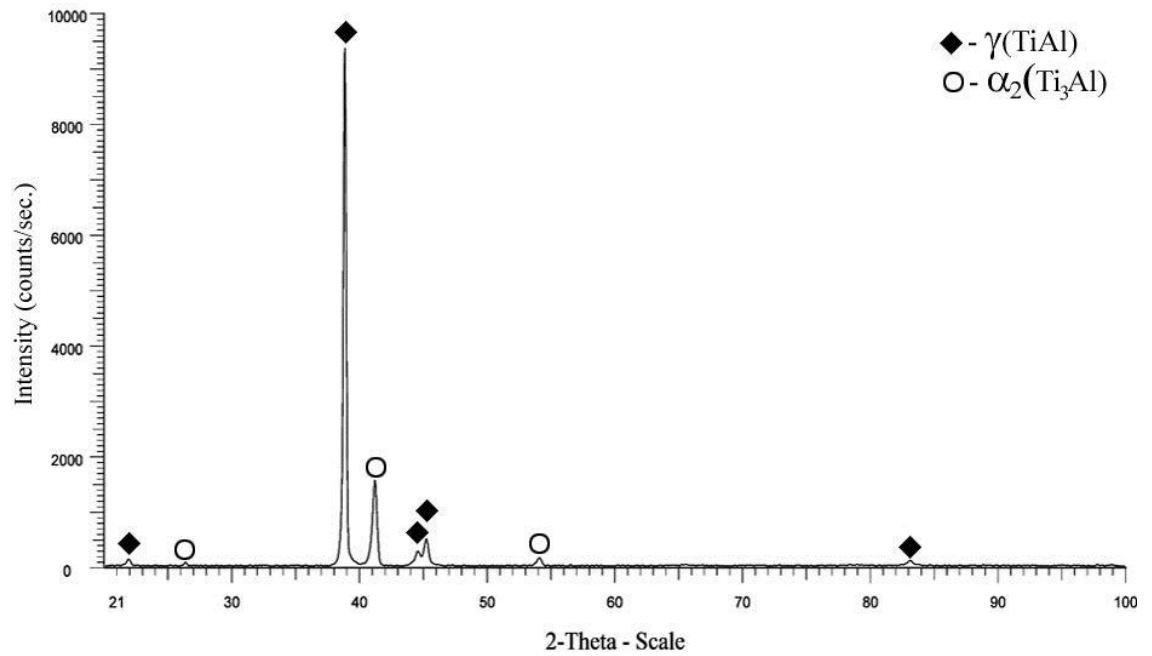


**Figure 4.7** XRD pattern of Ti-46Al-10Nb

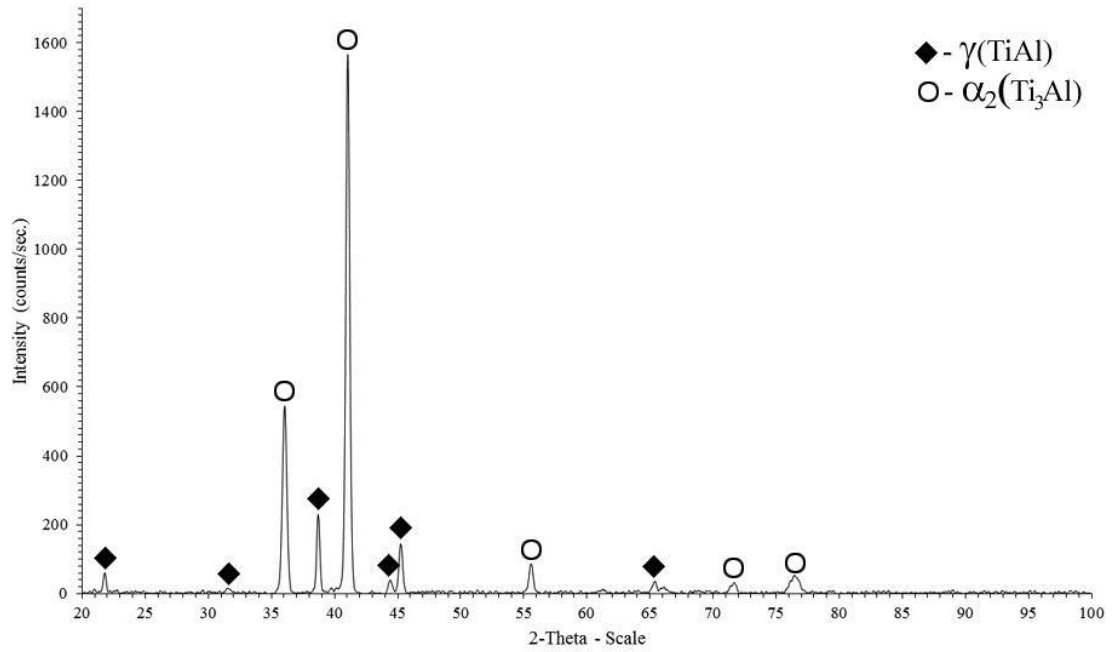


Figure 4.8 XRD pattern of Ti-48Al

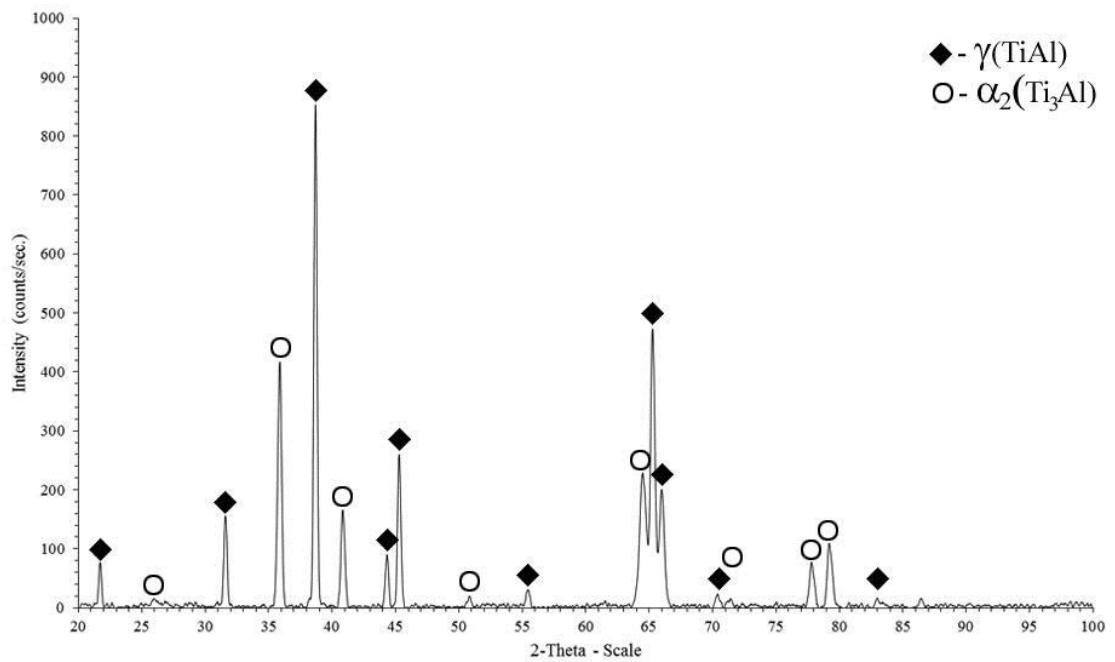
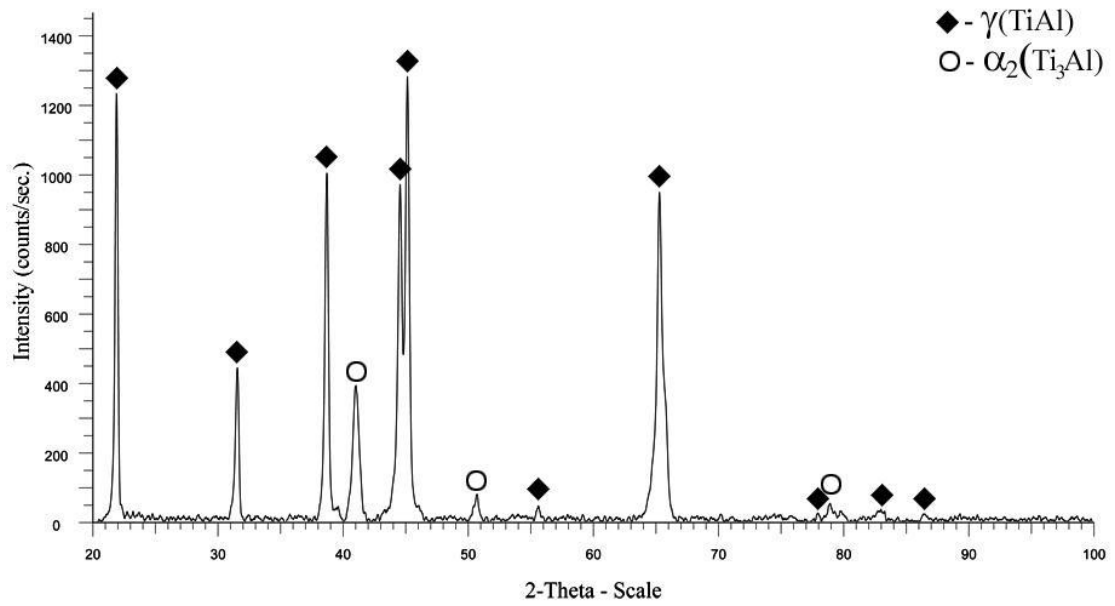


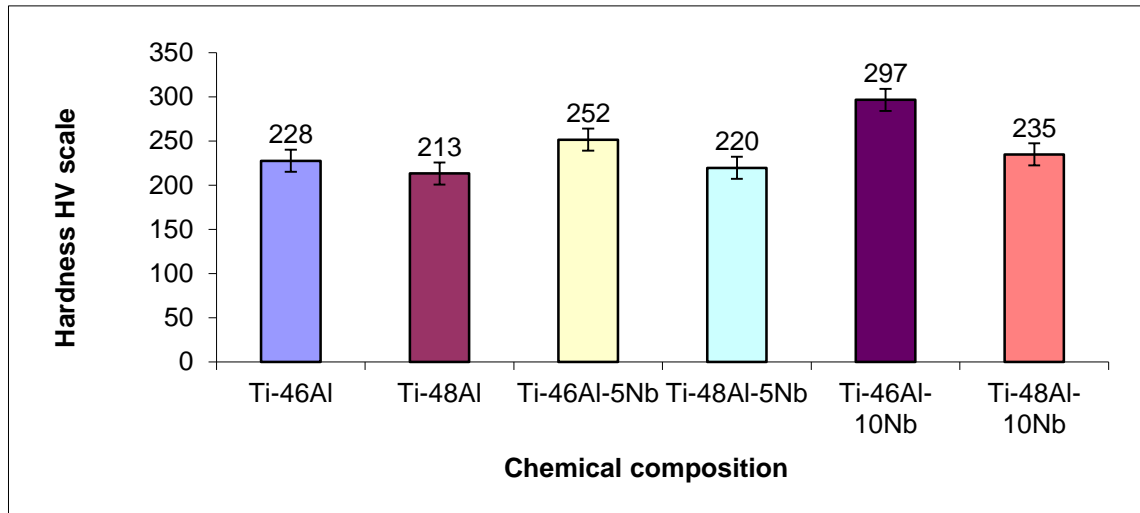
Figure 4.9 XRD pattern of Ti-48Al-5Nb



**Figure 4.10** XRD pattern of Ti-48Al-10Nb

### 4.1.3 Microhardness results

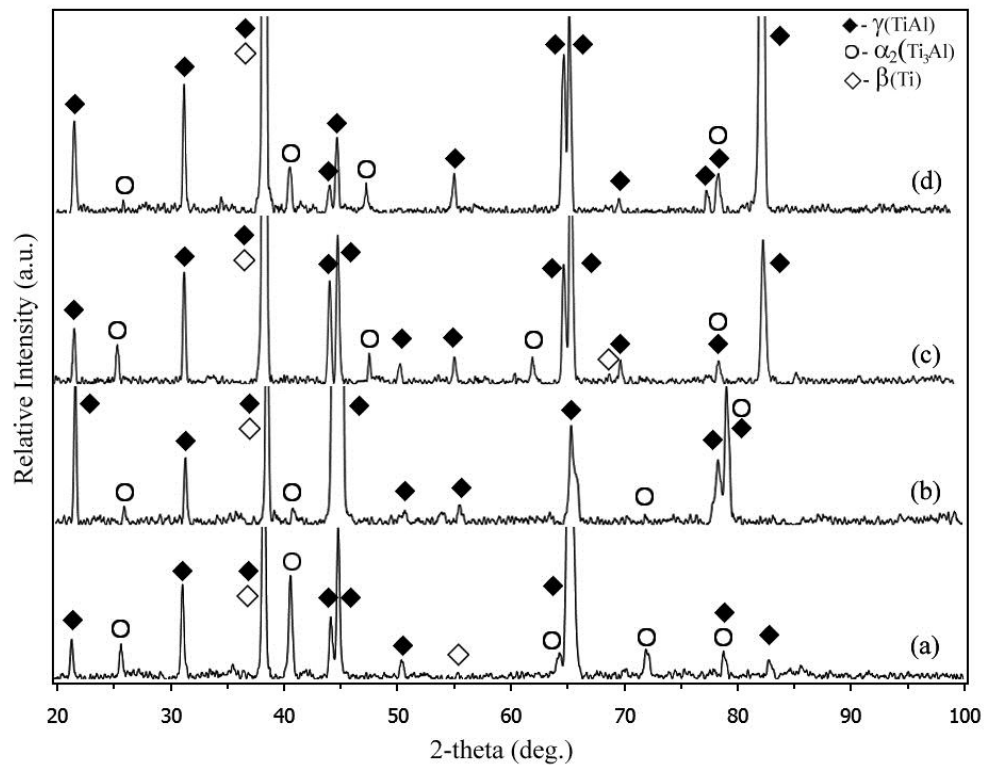
Figure 4.11 reports the results of microhardness measurements performed on the different alloys used in the present study. It is observed those possessing low aluminum content and Nb addition appears to be the harder. The Ti-46Al-10Nb alloy specimen shows a superior hardness (about 297 HV) when compared to those of other alloys due to higher aluminum content.



**Figure 4.11** Microhardness of experimental alloys

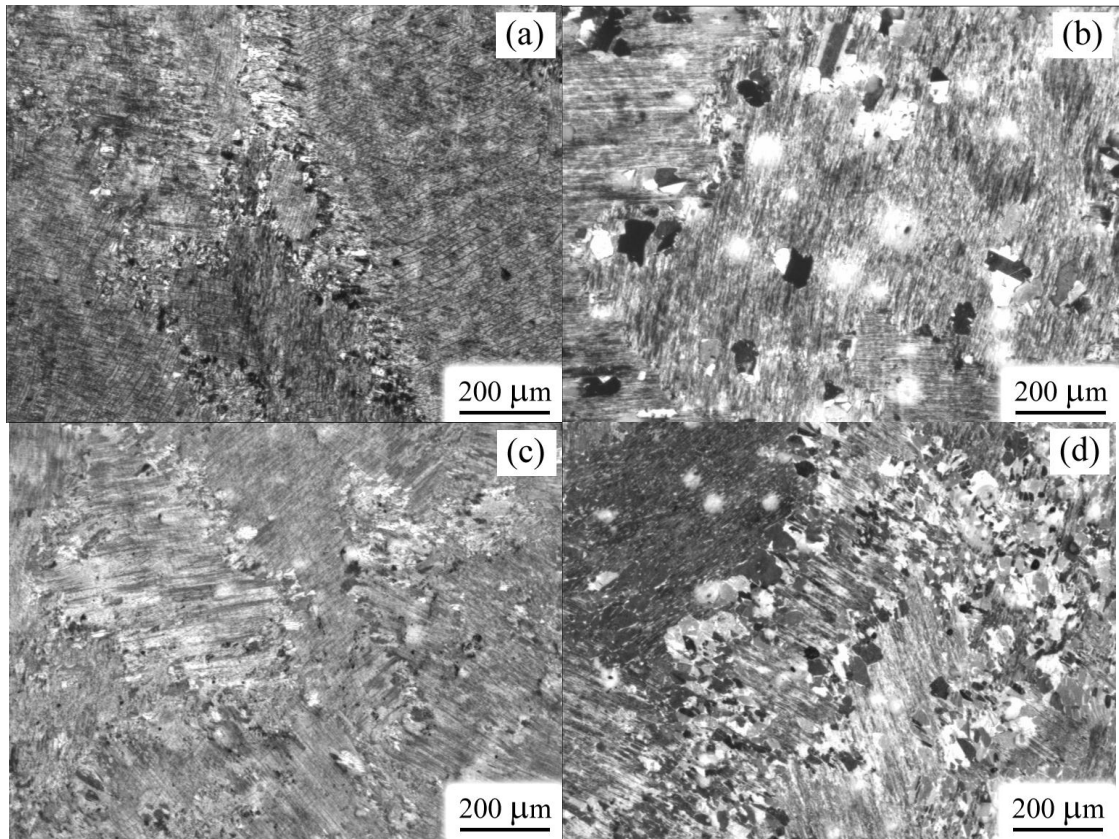
## 4.2 Solution-treated structures

Figure 4.12 shows the XRD patterns of Ti-46Al-2Mo, Ti-46Al-2Cr, Ti-46Al-4Nb-2Mo, and Ti-46Al-4Nb-2Cr samples prepared from solution treatment at 1400 °C for 30 min followed by air cooling. The results of the diffraction peak patterns indicated that the four alloys primarily consisted of  $\gamma$ -TiAl phase with small amounts of the  $\alpha_2$ -Ti<sub>3</sub>Al and  $\beta$  phases. Optical micrographs also confirmed the results obtained from the XRD patterns. The lamellar microstructure composed of alternating layers of  $\gamma$ ,  $\alpha_2$ , and  $\beta$  phases (Figure 4.13).



**Figure 4.12** X-ray diffraction patterns of the alloys after solution treatment:  
 (a) Ti-46Al-2Mo, (b) Ti-46Al-2Cr, (c) Ti-46Al-4Nb-2Mo and  
 (d) Ti-46Al-4Nb-2Cr

Inside the lamellar structure of each alloy (Ti-46Al-2Mo, Ti-46Al-2Cr, Ti-46Al-4Nb-2Mo, and Ti-46Al-4Nb-2Cr), a small volume fraction of equiaxed regions was observed (Figure 4.13 (a) - (d)). When the microstructures of all four alloys were compared, it was found that Ti-46Al-4Nb-2Cr alloy contained a larger content of equiaxed microstructure than the other three samples. Detailed observations of the BSE images of all four alloys are shown in Figure 4.14 (a) - (d) which reveals that the  $\beta$  phase was formed along the colony boundaries, distributed along the  $\gamma$  matrix.



**Figure 4.13** Microstructures of solution-treated alloys: (a) Ti-46Al-2Mo, (b) Ti-46Al-2Cr, (c) Ti-46Al-4Nb-2Mo, and (d) Ti-46Al-4Nb-2Cr

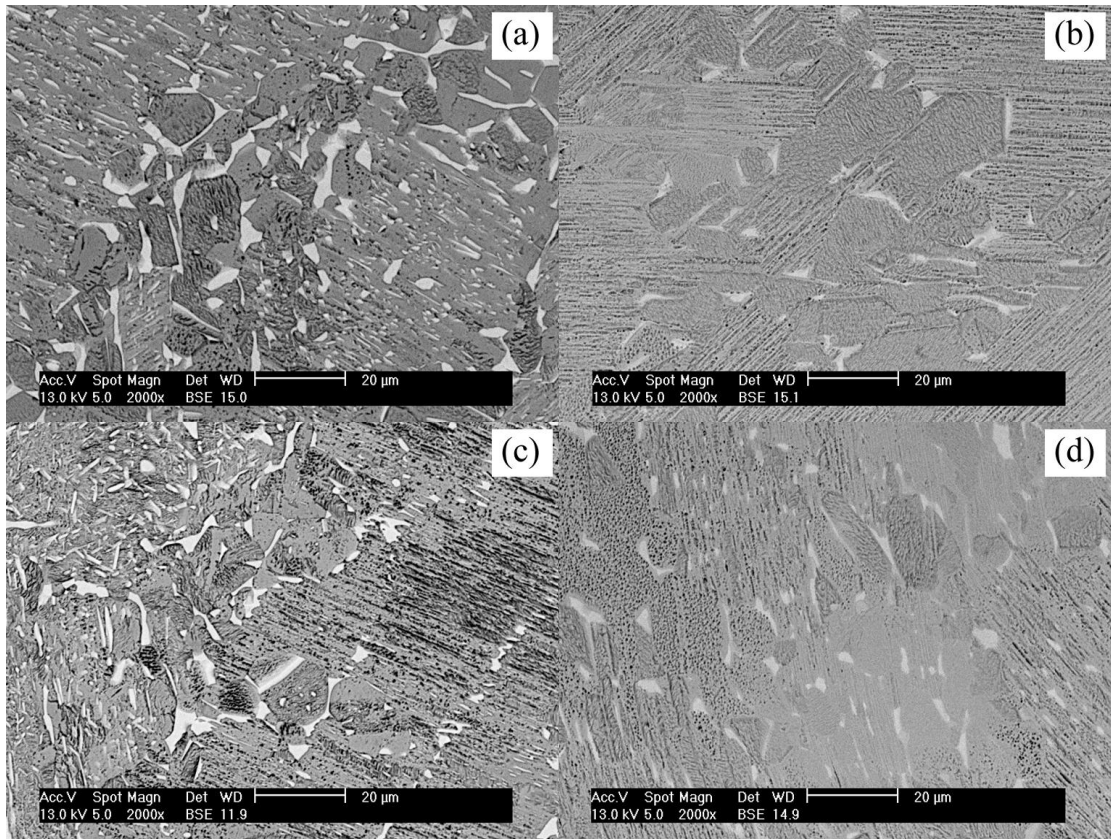


**Figure 4.14** BSE images showing  $\beta$ -phase in the four alloys: (a) Ti-46Al-2Mo, (b) Ti-46Al-2Cr, (c) Ti-46Al-4Nb-2Mo, and (d) Ti-46Al-4Nb-2Cr

### 4.3 Structures after the heat treatment

#### 4.3.1 Furnace-cooled treatment

After being heated at 1350°C for 1 h, the alloys were cooled in the furnace. Figure 4.15 shows the XRD patterns of all alloys (Ti-46Al-2Mo, Ti-46Al-2Cr, Ti-46Al-4Nb-2Mo, and Ti-46Al-4Nb-2Cr).  $\gamma$ -TiAl,  $\alpha_2$ -Ti<sub>3</sub>Al, and  $\beta$  phases were found in all alloys. Figure 4.16 shows the microstructures of all the alloys. It can be seen that Ti-46Al-2Mo and Ti-46Al-2Cr ternary alloys structures were composed of coarse  $\alpha_2 + \gamma$  fully lamellar grains with grain sizes of approximately 200-600 μm (Figure 4.16(a) and (b),

respectively). However, Ti-46Al-4Nb-2Mo and Ti-46Al-4Nb-2Cr quaternary alloy structures were found to possess smaller fractions of the  $\alpha_2 + \gamma$  lamellar structure than both of the ternary alloys. The grain sizes are approximately 50 – 200  $\mu\text{m}$  and 100 – 300  $\mu\text{m}$ , respectively. They also exhibit the occurrence of several equiaxed  $\gamma$ -monolithic grains (Figure 4.16(c) and (d)).

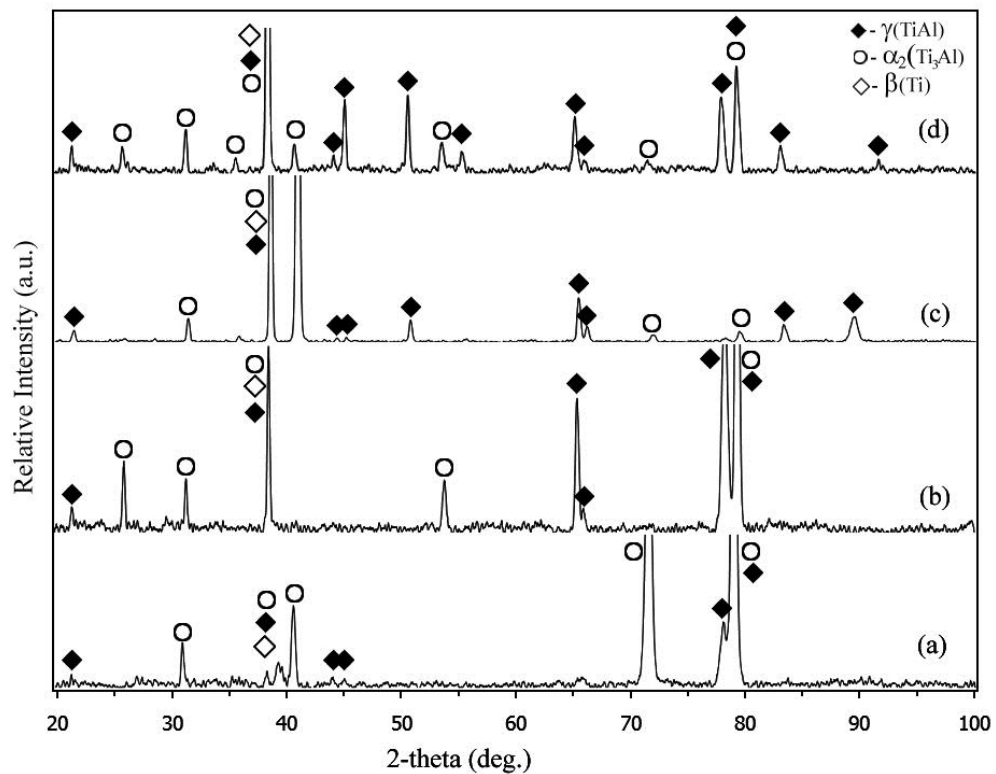


**Figure 4.15** X-ray diffraction patterns of furnace cooled alloys: (a) Ti-46Al-2Mo, (b) Ti-46Al-2Cr, (c) Ti-46Al-4Nb-2Mo and (d) Ti-46Al-4Nb-2Cr

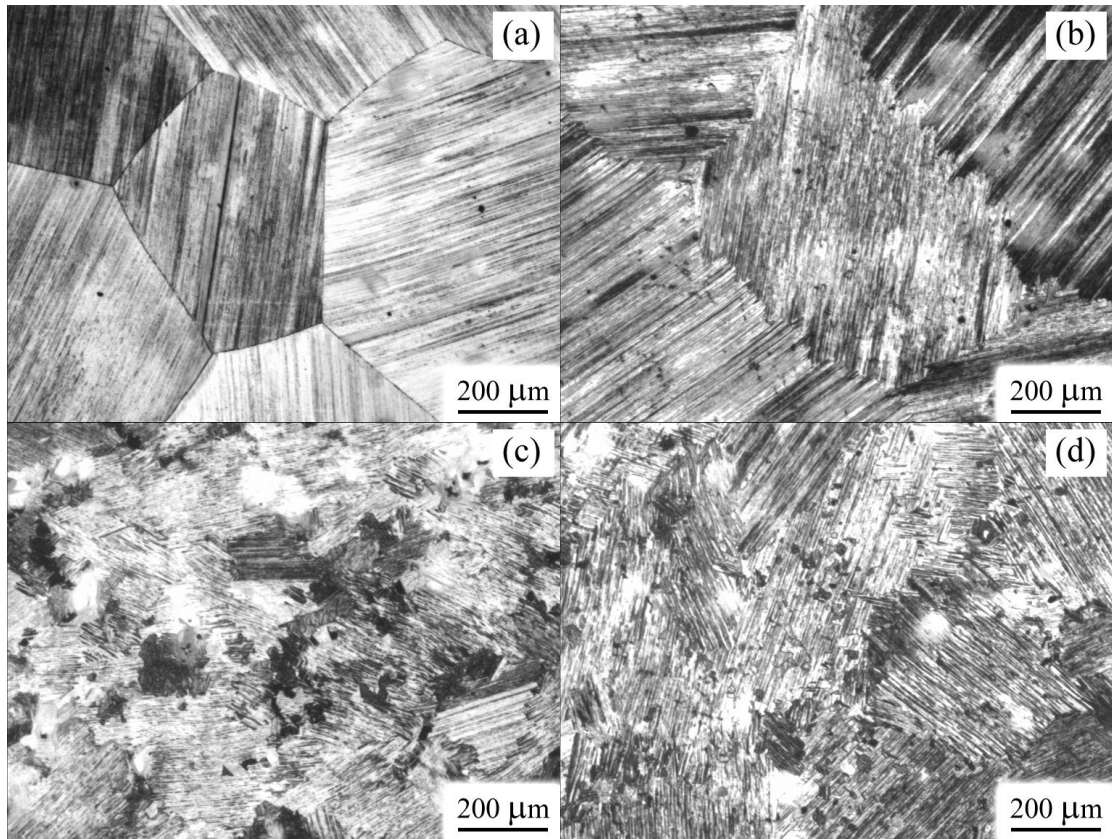


**Figure 4.16** Microstructures of furnace cooled alloys: (a) Ti-46Al-2Mo, (b) Ti-46Al-2Cr, (c) Ti-46Al-4Nb-2Mo, and (d) Ti-46Al-4Nb-2Cr

### 4.3.2 Air-cooled microstructures

The air-cooled structures revealed the presence of  $\alpha_2 + \gamma$  with small fractions of the  $\beta$  phase. This is in agreement with the findings from the XRD patterns shown in Figure 4.17. The microstructures of the air-cooled alloys are shown in Figure 4.18. The microstructure of Ti-46Al-2Mo alloy composed of  $\alpha_2 + \gamma$  lamellar grains with a size of approximately 200-350  $\mu\text{m}$ . The grain boundaries exhibited the Widmanstätten lath and feathery-like characteristics. In the case of the Ti-46Al-2Cr alloy, the microstructure displayed a fully lamellar structure with grain size of approximately 200-500  $\mu\text{m}$  (Figure 4.18(b)). There was a fine lath formation of  $\gamma$  phase arising at the edge of the grain boundary. Smaller grain size were observed in Ti-46Al-4Nb-2Mo alloy (Figure

4.18(c)), which contained  $\alpha_2 + \gamma$  lamellar grains with grain size of approximately 180-250  $\mu\text{m}$  and several equiaxed  $\gamma$ -monolithic grains (colony sizes of approximately 50-100  $\mu\text{m}$ ) distributed along the lamellar matrix. Interestingly, both of Ti-46Al-4Nb-2Cr (Figure 4.18(d)) and Ti-46Al-2Mo alloys (Figure 4.18(a)) have the same microstructure, and the  $\alpha_2 + \gamma$  lamellar grains are of the Widmanstätten lath and feathery-like structure at the grain boundaries. However, Ti-46Al-4Nb-2Cr alloy appeared to have smaller grain size (approximately 100-300  $\mu\text{m}$ ) and a lesser amount of the Widmanstätten lath and feathery-like (the structures attached to a grain boundary will henceforth be denoted as the “ $\gamma_{f-gb}$ ” structures shown in Figure 4.18(b)) structure at the grain boundaries than that of Ti-46Al-2Mo alloy.

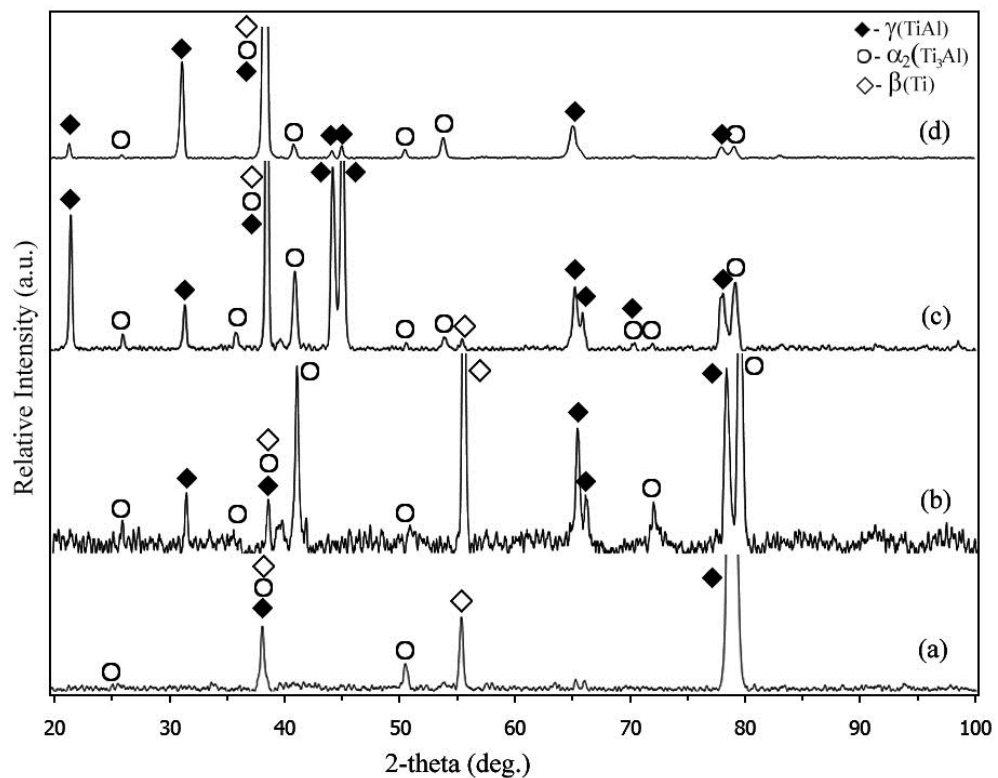


**Figure 4.17** X-ray diffraction patterns of the alloys prepared from the air cooled condition: (a) Ti-46Al-2Mo, (b) Ti-46Al-2Cr, (c) Ti-46Al-4Nb-2Mo and (d) Ti-46Al-4Nb-2Cr

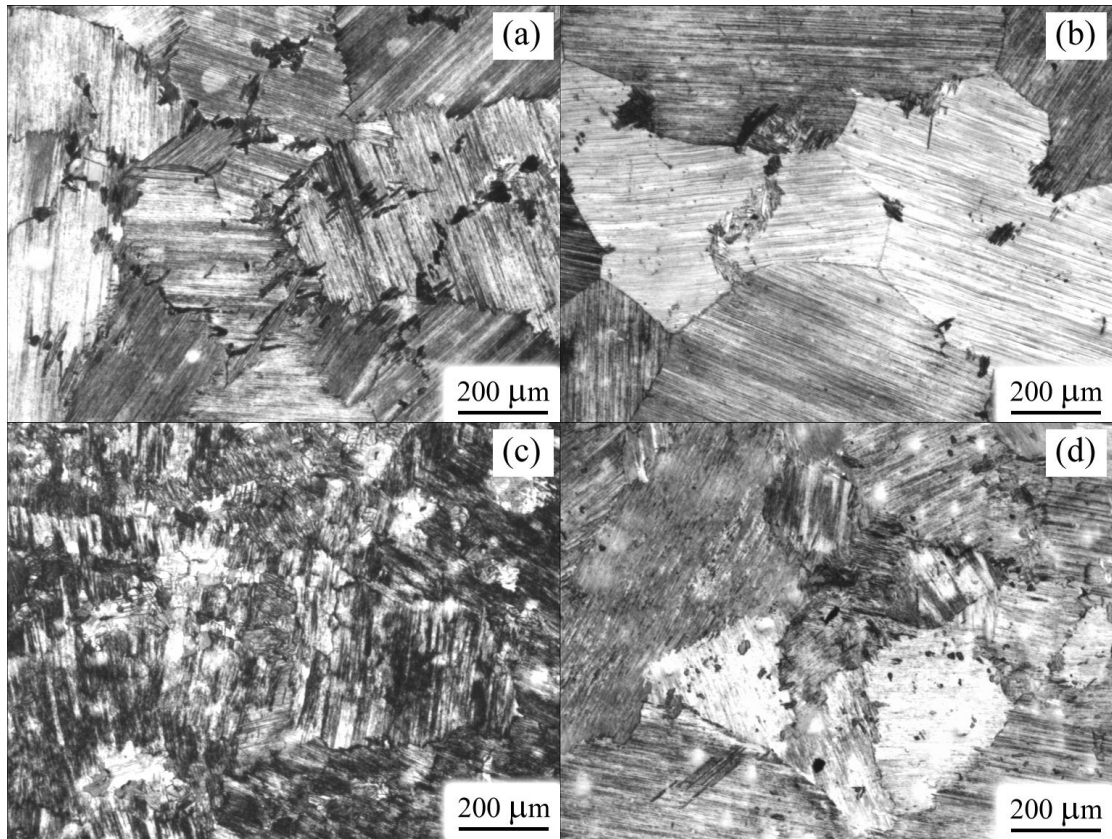


**Figure 4.18** Microstructures of the air cooled specimens: (a) Ti-46Al-2Mo, (b) Ti-46Al-2Cr, (c) Ti-46Al-4Nb-2Mo, and (d) Ti-46Al-4Nb-2Cr

### 4.3.3 Oil-quenched microstructures

The XRD patterns of the oil-quenched alloys are shown in Figure 4.19, and the structures of all alloys were in the  $\gamma+\alpha_2$  phase, revealing that no  $\beta$  phase was present. Figure 4.20 (a)-(d) shows the microstructures of the Ti-46Al-2Mo, Ti-46Al-2Cr, Ti-46Al-4Nb-2Mo, and Ti-46Al-4Nb-2Cr alloys received after the oil-quenched cooling. The Ti-46Al-2Mo alloy microstructure consisted of lamellar  $\gamma$  phase (with a volume fraction of approximately 45 %) which was present on the bright  $\alpha_2$ -massive matrix and several  $\gamma$  phase precipitate regions (black) (Figure 4.20(a)). Figure 4.20 (b) reveals the large-grained microstructure of the Ti-46Al-2Cr alloy which mainly consisted of a

lamellar structure of  $\gamma+\alpha_2$  phases with significant  $\alpha_2$ -massive regions. The colony sizes ranged from 350 to 500  $\mu\text{m}$ .

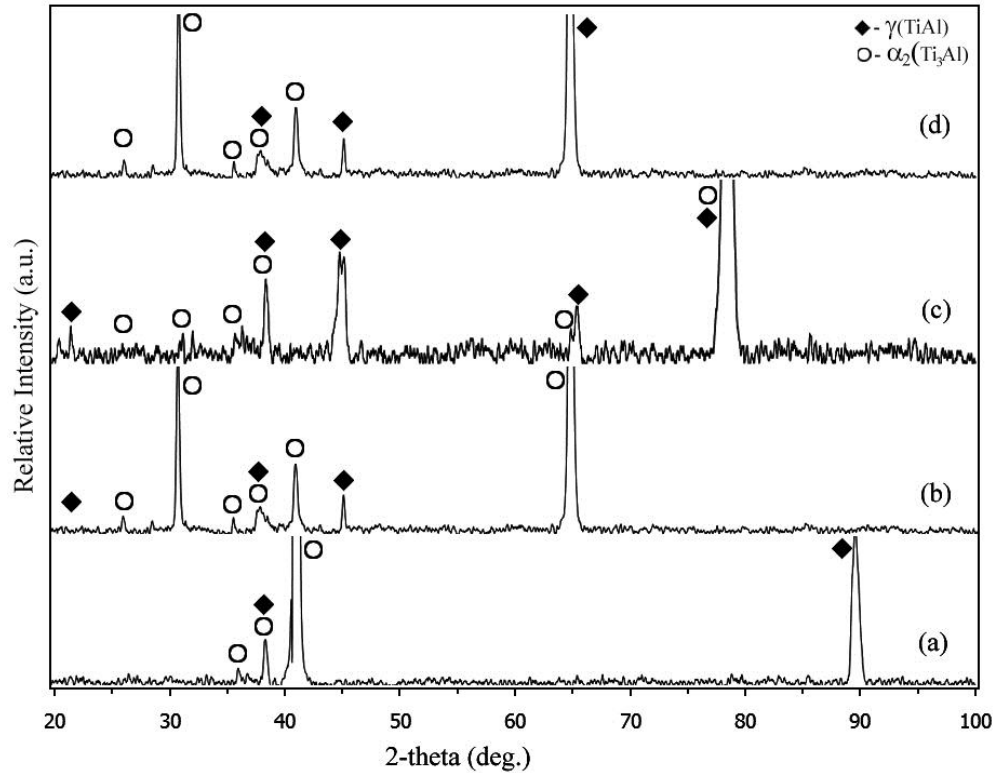


**Figure 4.19** X-ray diffraction patterns of the alloys prepared from the oil quenched condition: (a) Ti-46Al-2Mo, (b) Ti-46Al-2Cr, (c) Ti-46Al-4Nb-2Mo and (d) Ti-46Al-4Nb-2Cr

The transformation of this lamellar morphology started at the grain boundaries and grew into the grain interiors. The structure of Ti-46Al-4Nb-2Mo alloys exhibited a random distribution of several regions of massively transformed  $\gamma$  phase (dark regions). These regions were visible within the main  $\alpha_2$ -bright matrix, as can be seen in Figure 4.20(c). In the micrographs, it is evident that the microstructures of both alloys mostly exhibited the significant contents of  $\alpha_2$ -massive grains ( $\alpha_2\text{m}$ ). These grains were transformed from the disordered  $\alpha$  phase (a diffusionless transformation above the eutectoid temperature). Additionally, a lesser amount of  $\gamma$ -massive structure was located mainly at the grain

boundaries with colony sizes of approximately 100-200  $\mu\text{m}$ . The volume fraction of the massively transformed  $\gamma$  phase was measured to be approximately 40 %. The last alloy depicted is an oil-quenched Ti-46Al-4Nb-2Cr with the micrograph shown in Figure 4.20 (d).

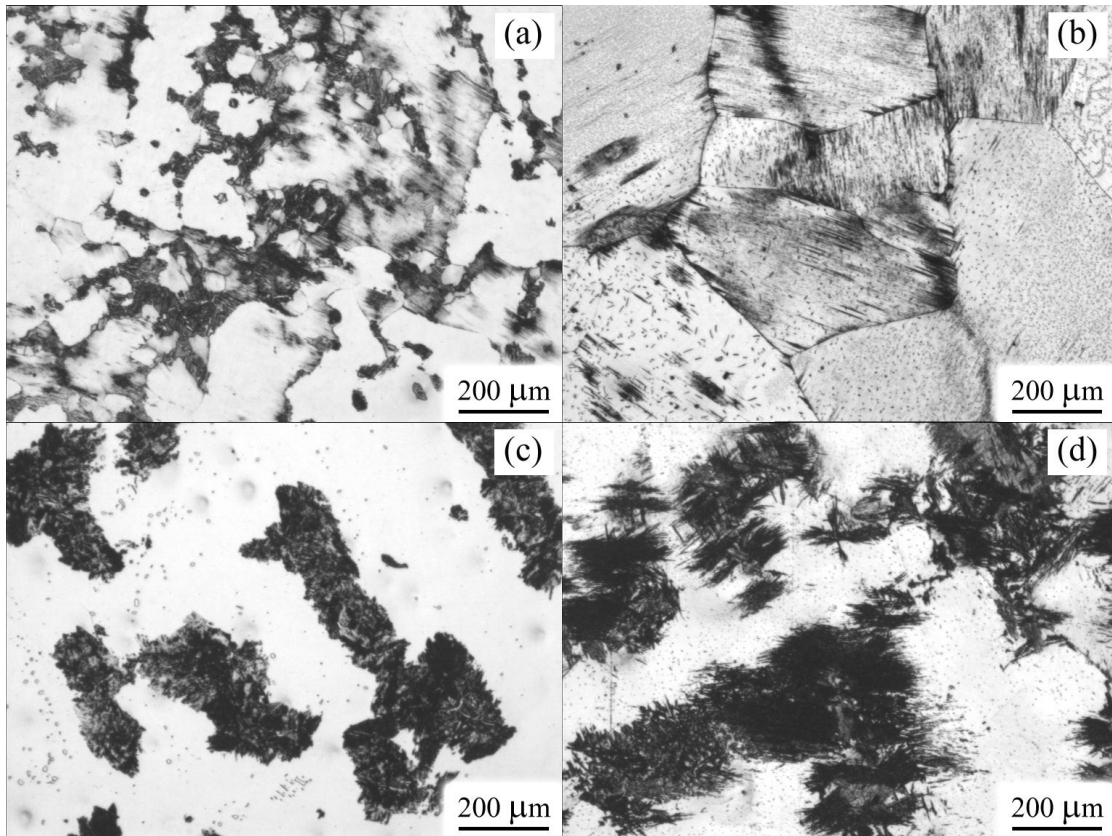


**Figure 4.20** Microstructures of the oil quenched alloys: (a) Ti-46Al-2Mo, (b) Ti-46Al-2Cr, (c) Ti-46Al-4Nb-2Mo, and (d) Ti-46Al-4Nb-2Cr

#### 4.3.4 Water-quenched microstructures

The structures of water-quenched Ti-46Al-2Mo, Ti-46Al-2Cr, Ti-46Al-4Nb-2Mo, and Ti-46Al-4Nb-2Cr alloys are revealed in the XRD patterns shown in Figure 4.21. The structure of Ti-46Al-2Mo was found to contain only  $\alpha_2$ -massive with a small content of

$\gamma$  phase. For the remaining four alloys (the Ti-46Al-2Mo, Ti-46Al-2Cr, Ti-46Al-4Nb-2Mo, and Ti-46Al-4Nb-2Cr alloys), the peaks indicated the presence of the  $\alpha_2 + \gamma$  phase.

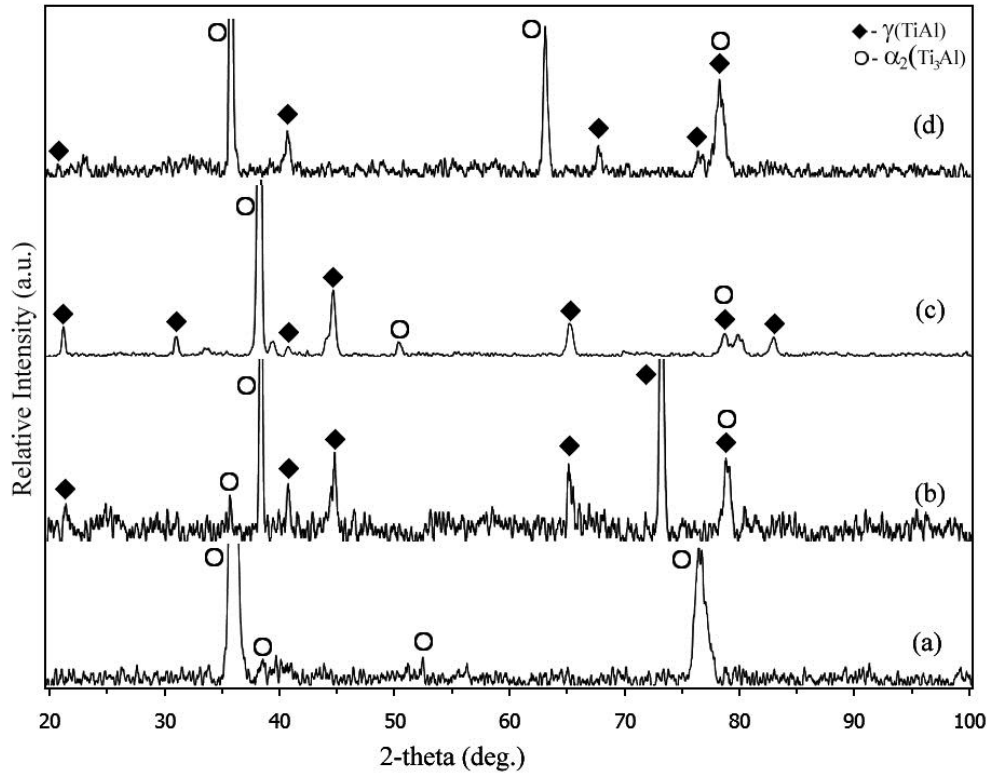


**Figure 4.21** X-ray diffraction patterns of the alloys in the water quenched condition:

(a) Ti-46Al-2Mo, (b) Ti-46Al-2Cr, (c) Ti-46Al-4Nb-2Mo, and (d) Ti-46Al-4Nb-2Cr

The microstructures of alloys after the heat treatment and the water-quenching are shown in Figure 4.22. For the microstructure of Ti-46Al-2Mo alloy (Figure 4.22(a)), small patch clusters (dark regions) can be seen in bright  $\alpha_2$ -massive matrix. This implies that the massive  $\gamma$  distribution occurred occasionally in the alloy. The microstructure of Ti-46Al-2Cr case was similar to that of Ti-46Al-2Mo alloy with little difference in the quantity and features of the phases. As can be seen in Figure 4.22(b), in comparison to the Ti-46Al-2Mo alloy, the Ti-46Al-2Cr microstructure exhibited a featureless bright  $\alpha_2$

matrix with fine acicular patches and approximately 15% (dark regions) volume fraction of the massive  $\gamma$  structure (colony sizes of approximately 100-200  $\mu\text{m}$ ). Microcracks were also found in the  $\alpha_2$  matrix. The water-quenched microstructure of the Ti-46Al-4Nb-2Mo alloy (Figure 4.22(c)) was the same as that of Ti-46Al-2Mo alloy microstructure, which contained the massive  $\gamma$  structure (the dark areas) in the  $\alpha_2$ -massive matrix (the white background); however, the amount and the volume fraction (approximately 21%) of  $\gamma$ -massive structure was both less than that of Ti-46Al-2Mo alloy.

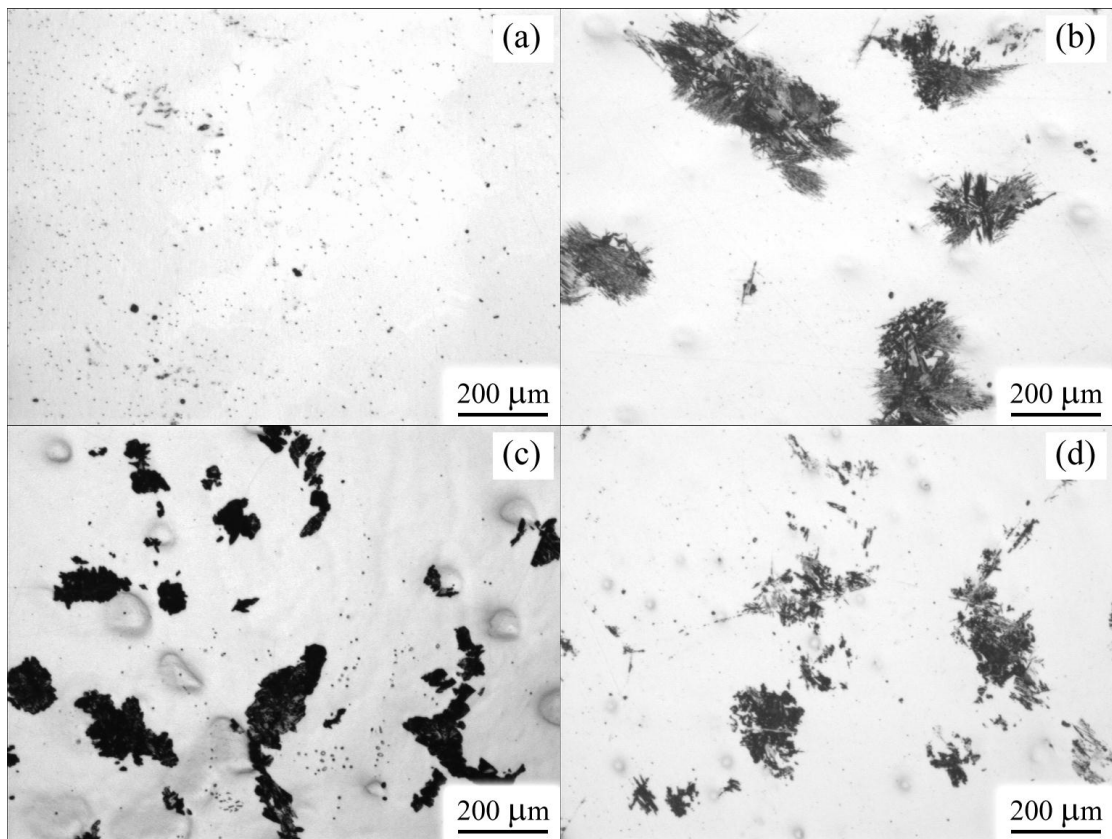


**Figure 4.22** Microstructures of water quenched alloys: (a) Ti-46Al-2Mo, (b) Ti-46Al-2Cr, (c) Ti-46Al-4Nb-2Mo, and (d) Ti-46Al-4Nb-2Cr

Microstructure of water-quenched Ti-46Al-4Nb-2Cr alloy is illustrated in Figure 4.22(d). which shows that the microstructure is composed of light and fine acicular patches of massive  $\gamma$  structure, both inside the featureless bright  $\alpha_2$ -massive( $\alpha_{2m}$ ) matrix and at the  $\alpha_{2m}$  grain boundaries (the colony sizes are approximately 30-200  $\mu\text{m}$ ). The volume fraction of the massive phase was approximately 12 % (dark regions). Comparing to the microstructures of all four alloys (Ti-46Al-2Mo, Ti-46Al-2Cr, Ti-46Al-4Nb, and Ti-46Al-4Nb-2Cr), it was found that some alloys exhibited similar microstructures. However, microstructures of the water quenched alloys were very different from those of the alloys cooled in the furnace and in air.

For massive transformation that resulted in the oil- and water-quenched sample Ti-46Al-2Cr sample were selected to confirm that the massive phase transformation occurred without any large-scale compositional changes. The results of chemical distribution within  $\alpha_2$ -matrix and  $\gamma$ -massive phase were identified with line scan technique by EDS, and the chemical composition results confirm that Ti, Al, and Cr elements were distributed equally within the area analyzed, as shown in Figure 2.23.

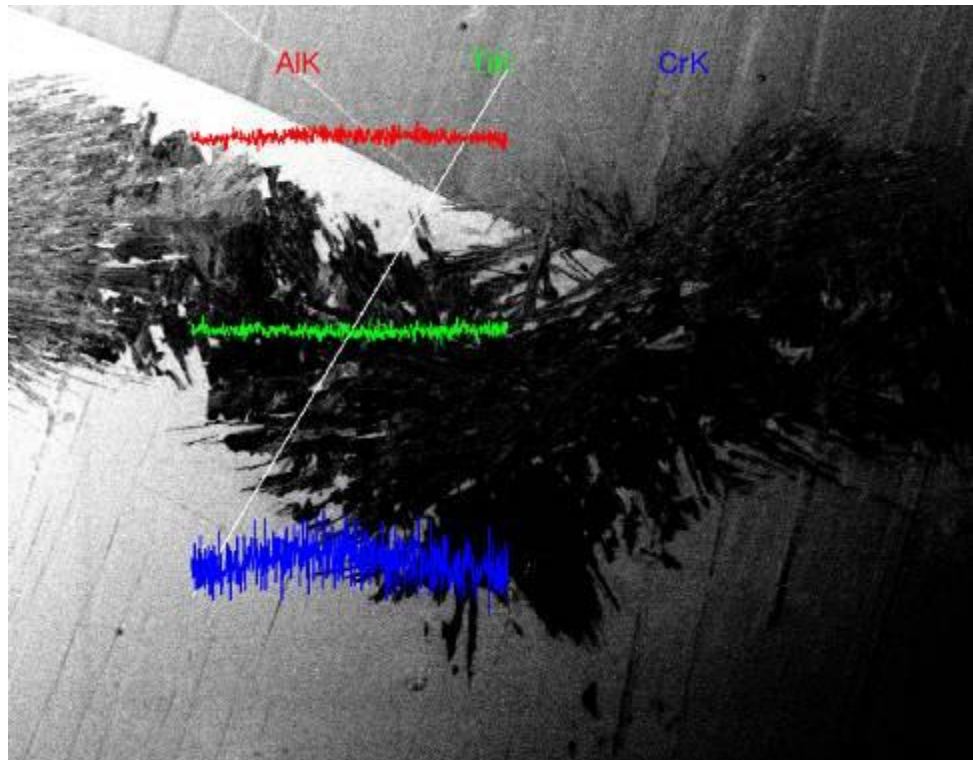


**Figure 2.23** EDS results for chemical composition analysis

#### 4.4 Electron Back-Scatter Diffraction analysis results

In this section, the relationship between the parent phase and the product phase was investigated. Two samples were selected to for investigations were Ti-46Al-4Nb-2Mo and Ti-46Al-4Nb-2Cr alloys. The electron back-scatter diffraction (EBSD) results for the Ti-46Al-4Nb-2Mo sample quenched in oil are shown in Figure 4.24. Figure 4.24(a) shows a BSE image of the massive- $\gamma$  structure and Figure 4.24(b) shows an EBSD image showing that the massive- $\gamma$  was associated with gamma in the lamellae form (subgrain 1). Together, these images demonstrate that the massive- $\gamma$  transformation was associated with gamma in the lamellar- $\gamma$  form. The EBSD image in Figure 4.24 (c) shows that there were different orientations between lamellar- $\gamma$  (labeled 1) and

massively transformed- $\gamma$  (labeled 2) regions. In considering the two regions displayed in the image, it can be concluded that their orientation were not dependent. Moreover, the Kikuchi maps, shown in Figure 4.24 (d), confirm that the massive- $\gamma$  in subgrain 2 had the same orientation as the lamellar- $\gamma$  in subgrain 1. The stereograms presented in Figure 4.24 (e) reveals information regarding the orientation relationship of subgrain 1 to subgrain 2, and it is evident that subgrain 1 is in fact related to subgrain 2. The relationship between the two subgrains is an example of the twin phenomenon, which has been report by Dey et al. [40]. Indeed, the growth of the massive structure was promoted by low-stacking-fault energy and twinning that occurred over the  $\{111\}$  plane.

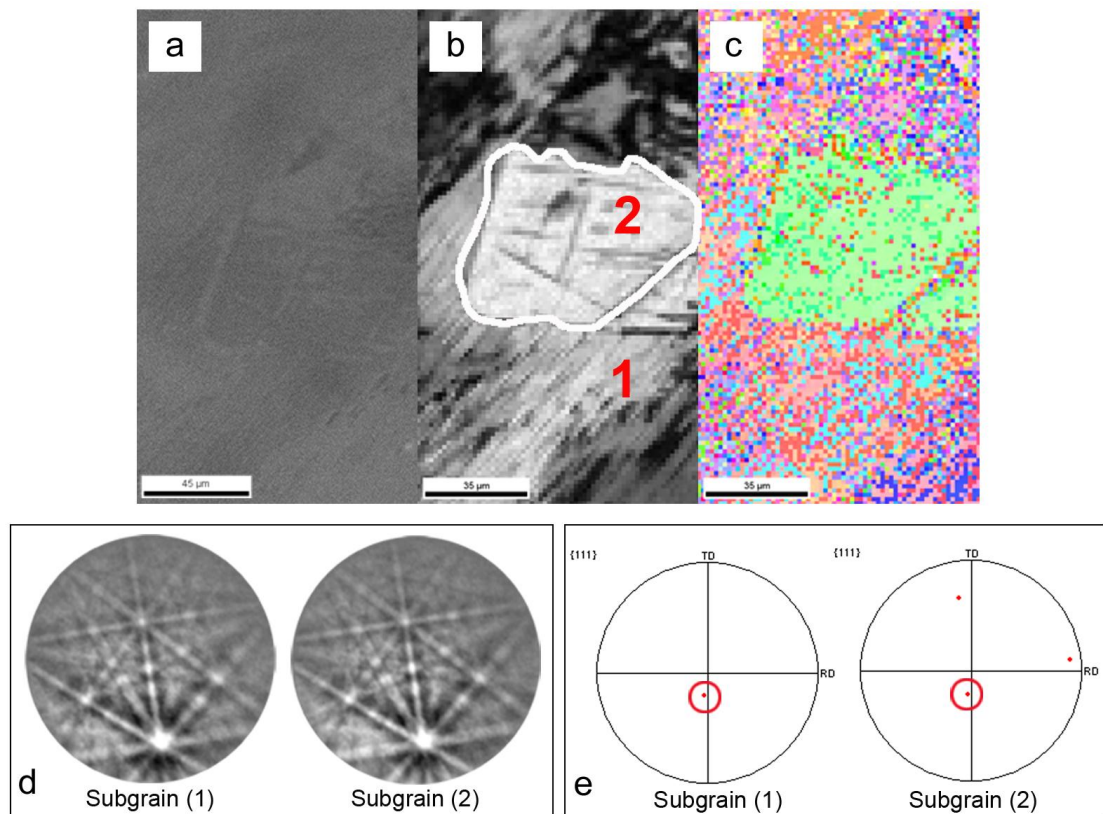


**Figure 4.24** Micrographs and diffraction patterns from a sample of Ti-46Al-4Nb-2Mo, oil quenched from 1,350°C.

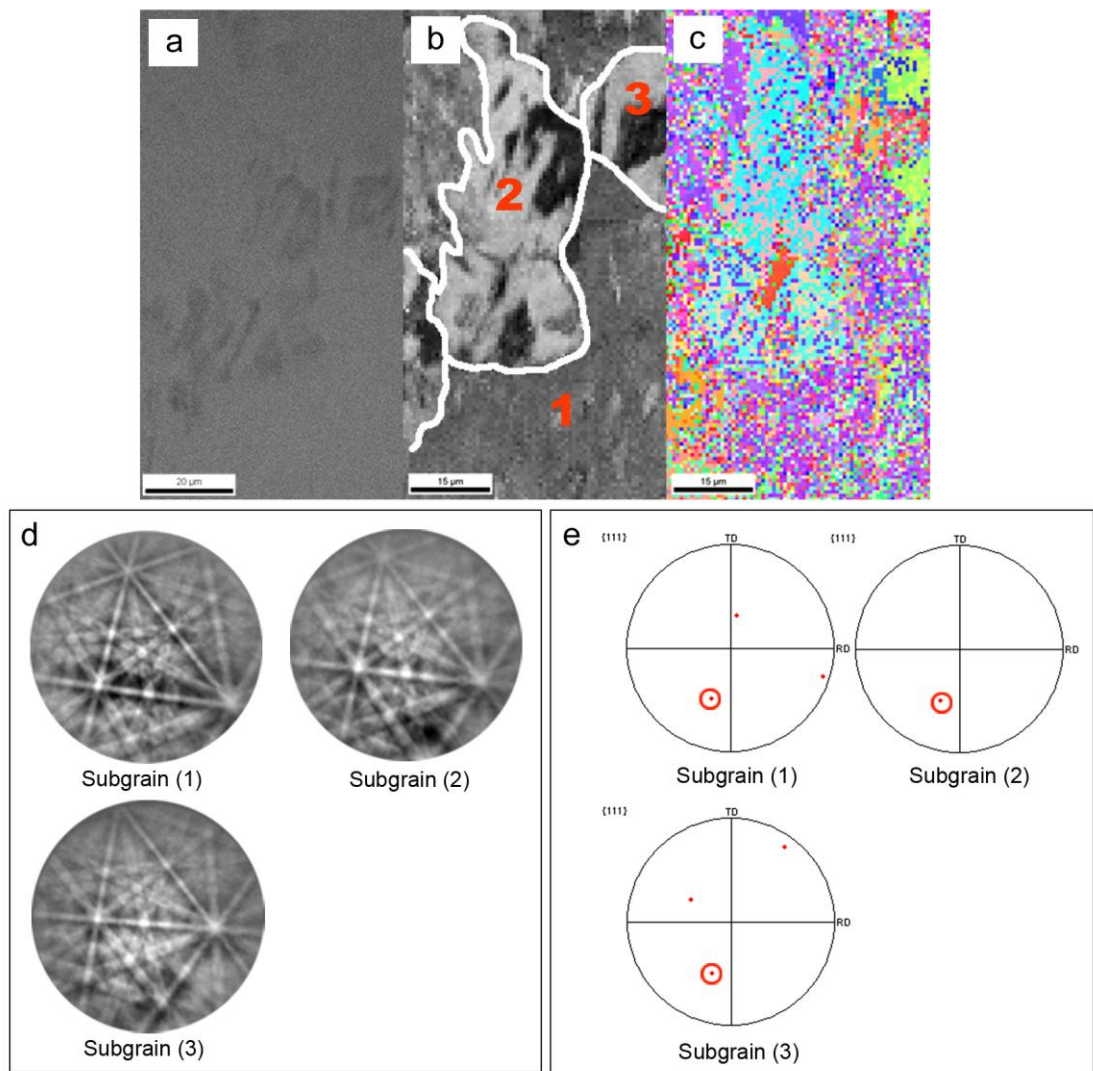


**Figure 4.25** Micrographs and diffraction patterns from a sample of Ti-46Al-4Nb-2Cr which was oil quenched from 1,350°C.

Figure 4.25(a) shows an EBSD image of the massive- $\gamma$  structure of the Ti-46Al-4Nb-2Cr oil quenched sample. Figure 4.25(b) shows the difference between the two regions, one as a dark area and the other light, which indicate the occurrence of massive- $\gamma$ . The EBSD image in Figure 4.25(c) explains the orientation relationships of subgrain 1, subgrain 2 and subgrain 3. The overall results of the microstructures in the three subgrains revealed the massive- $\gamma$  transformed structure. The orientation relationships of

all three subgrains, based on the Kikuchi maps shown in Figure 4.25(d), were confirmed to be the massively transformed structure within subgrain 2 and subgrain 3, which nucleated from the twin-related regions in subgrain 1 along the (111) plane. The orientation relationships were also confirmed by the pole figure given in Figure 4.25(e).

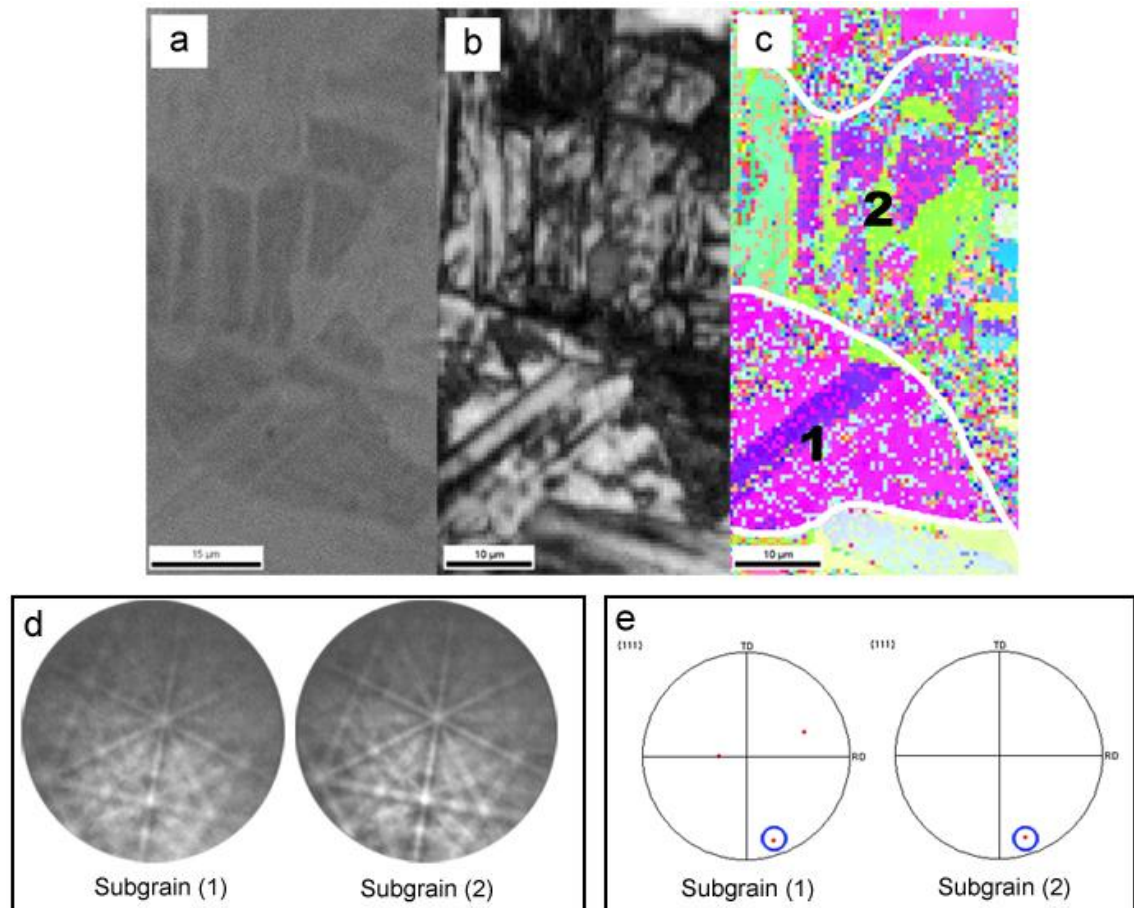


**Figure 4.26** Micrographs and diffraction patterns from a sample of Ti-46Al-4Nb-2Mo water quenched from 1,350°C.

Figure 4.26 shows the microstructure of water quenched Ti-46Al-4Nb-2Mo. The EBSD images in Figure 4.26 (a)-(c) show the components of the lamellar structure (region 1) and the massive- $\gamma$  structure (region 2). These findings are based on the identifications of the colored regions in the EBSD image and on the associated pole figures and

corresponding Kikuchi maps, which are shown in Figure 4.26 (c)-(e). The Kikuchi maps shown in Figure 4.26 (d) confirm that the massive- $\gamma$  in region 2 has an identical orientation to the lamellae present in region 1. The stereograms given in 4.26 (e) are of the lamellar and massive- $\gamma$  regions, showing that the massive- $\gamma$  in region 2 is parallel with the (111) in region 2 and the twin-related to region 1 with the (111) plane.

The water quenched samples of Ti-46Al-4Nb-2Cr sample exhibited a massive- $\gamma$  transformation (Figure 4.27 (a)-(d)). The microstructure of Ti-46Al-4Nb-2Cr samples showed a similar transformation to that in the previous case (Ti-46Al-4Nb-2Mo). However, the Ti-46Al-4Nb-2Cr sample showed a clear nucleation site of the massive- $\gamma$  formation. Figure 4.27 (b) shows that the massive- $\gamma$  was nucleated at the grain boundary and then grew into the parent phase (as a small island). Additionally, there was more structural contrast in the two regions. The  $\{111\}$  pole figure and Kikuchi maps given in Figure 4.27 (d) and (e) show that the massive- $\gamma$  (region 1) and alpha parent phase (region 2) had the same orientation relationship. Indeed, the matrix (0001) of the alpha parent phase was parallel with the (111) plane in region 1 of the massive- $\gamma$ .

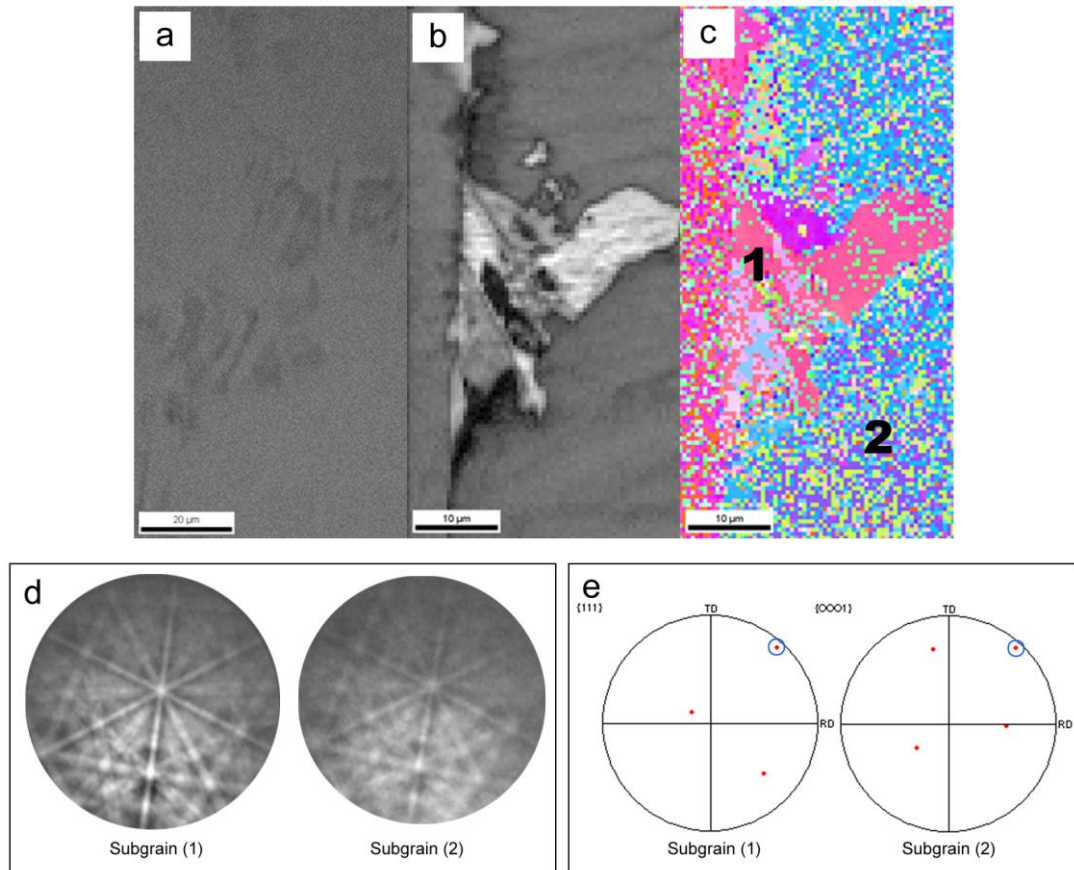


**Figure 4.27** Micrographs and diffraction patterns from a sample of Ti-46Al-4Nb-2Cr water quenched from 1,350°C.

#### 4.5 Microhardness results

Microhardness tests of the four alloys from various cooling conditions were performed and the results are shown in Figure 4.28. Comparisons of the results revealed that solution treated Ti-46Al-2Cr and Ti-46Al-4Nb-2Cr alloys had nearly the same hardness values, approximately  $298 \pm 21$  and  $299 \pm 12$  HV, respectively. The other two alloys, Ti-46Al-2Mo and Ti-46Al-4Nb-2Mo, exhibited the hardness of approximately  $322 \pm 19$  and  $326 \pm 17$  HV, respectively. In the furnace cooled conditions, Ti-46Al-2Cr alloy demonstrated the lowest microhardness at approximately  $284 \pm 14$  HV, while the

remaining three alloys, Ti-46Al-2Mo, Ti-46Al-4Nb-2Mo, and Ti-46Al-4Nb-2Cr, possessed microhardness values of approximately  $339\pm 19$ ,  $322\pm 21$ , and  $311\pm 12$  HV, respectively. In the oil-quenched condition, Ti-46Al-2Mo and Ti-46Al-2Cr alloys had microhardness values higher than those of the other two alloys, at  $456\pm 11$  and  $462\pm 18$  HV, respectively, while Ti-46Al-4Nb-2Mo and Ti-46Al-4Nb-2Cr alloys had microhardnesses of  $386\pm 13$  and  $434\pm 17$  HV, respectively. For the water quenched alloys, the microhardness values of the four alloys were approximately the same, in the range of 438-458 HV. Of these, Ti-46Al-4Nb-2Mo alloy had the highest value ( $458\pm 15$  HV), and the lowest value was observed for the Ti-46Al-4Nb-2Cr alloy, at approximately  $438\pm 11$  HV.

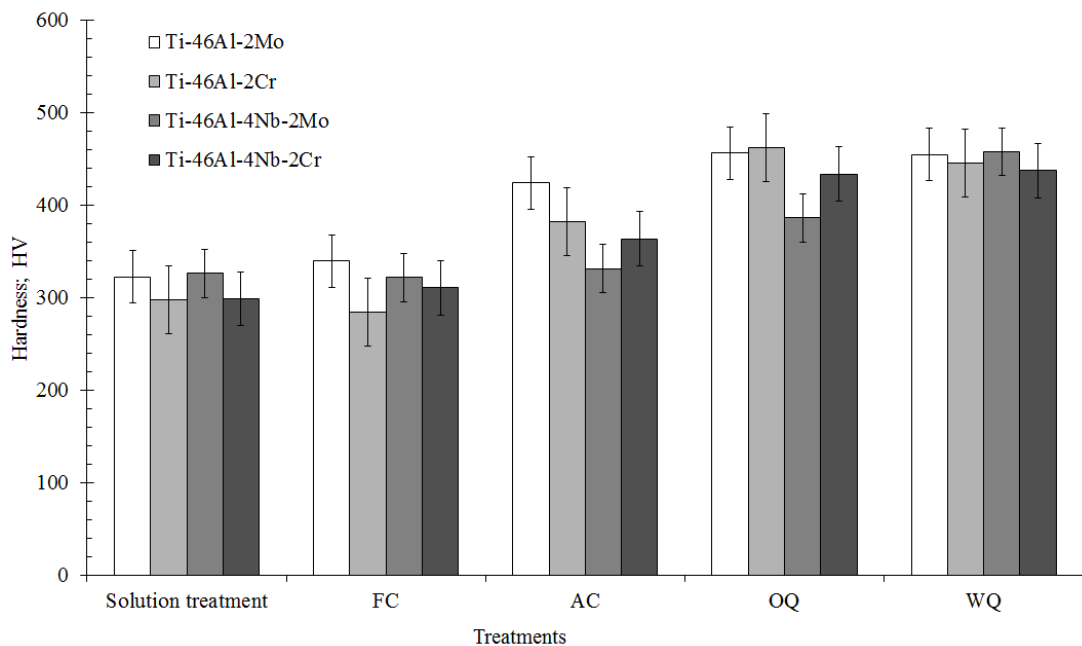


**Figure 4.28** Variations in the microhardness of the TiAl alloy samples under the different treatment conditions